PHYSICS

Nanoscale magnetic imaging using circularly polarized high-harmonic radiation

Ofer Kfir,[1,2*†] Sergey Zayko,[1*] Christina Nolte,[3] Murat Sivis,[1] Marcel Möller,[1] Birgit Hebler,[4] Sri Sai Phani Kanth Arekapudi,[4] Daniel Steil,[3] Sascha Schäfer,[1] Manfred Albrecht,[4] Oren Cohen,[2] Stefan Mathias,[3,5] Claus Ropers[1,5†]

Copyright © 2017 The Authors, some rights reserved; exclusive licensee American Association for the Advancement of Science. No claim to original U.S. Government Works. Distributed under a Creative Commons Attribution NonCommercial License 4.0 (CC BY-NC).

This work demonstrates nanoscale magnetic imaging using bright circularly polarized high-harmonic radiation. We utilize the magneto-optical contrast of worm-like magnetic domains in a Co/Pd multilayer structure, obtaining quantitative amplitude and phase maps by lensless imaging. A diffraction-limited spatial resolution of 49 nm is achieved with iterative phase reconstruction enhanced by a holographic mask. Harnessing the exceptional coherence of high harmonics, this approach will facilitate quantitative, element-specific, and spatially resolved studies of ultrafast magnetization dynamics, advancing both fundamental and applied aspects of nanoscale magnetism.

INTRODUCTION

Nanoscale magnetic structures exhibit a rich variety of patterns, textures, and topological states (*1*, *2*), governed by the complex interplay of multiple spin-coupling mechanisms (*3*). Mapping such spin configurations and their dynamic response is essential for the development of functional nanomagnetic systems (*4*–*10*). Magnetic imaging with high spatial and ultrafast temporal resolution is possible using circularly polarized extreme ultraviolet (EUV) and soft x-ray radiation. However, short-wavelength magneto-optical microscopy (*7*, *10*) is presently limited to synchrotrons and free-electron lasers (FELs), although recent developments in polarization-controlled high-harmonic generation promise a laboratory-scale implementation (*11*, *12*).

High-order harmonic generation (HHG) (*13*) is a process that gives rise to spatially and temporally coherent EUV (*14*) and soft x-ray beams with unique features. The spectral bandwidth of high-harmonic radiation supports attosecond pulses (*15*, *16*) and can be used to probe multiple chemical elements (*17*, *18*) or to create stable EUV frequency combs (*19*). Imaging experiments using high-harmonic radiation (*20*–*23*) benefit from the source's coherence, which enables high spatial resolution at a large field of view (*24*, *25*). High-harmonic imaging has consistently proven capable of nanoscale resolution for high-contrast, lithographically produced objects. On the other hand, the mapping of chemical and electronic contrast, polarization anisotropies (*26*), chiral features, or spin textures has remained challenging, despite a great potential for applications. In particular, the spectral region accessible by high harmonics spans the magneto-optical activity range of widely used ferromagnetic materials, facilitating, for example, spectroscopic (*17*) or diffractive (*27*) probing of ultrafast magnetism.

Generally, magneto-optical imaging with EUV and x-ray radiation combines element specificity and an in situ compatibility with currents or strong electric and magnetic fields (*28*), which has allowed for dynamical studies of domain walls (*29*), magnetic vortices (*7*), and skyrmions (*10*). Full-field magneto-optical imaging was pioneered by Eisebitt *et al.* (*30*), using Fourier transform holography (FTH) (*31*). In this scheme, x-ray magnetic circular dichroism (XMCD) provides phase and amplitude contrast of the magnetization component parallel to the circularly polarized x-ray beam. Because the magneto-optical contrast (*32*) is typically weak and suffers from nonmagnetic absorption, to date, XMCD-based microscopy is available exclusively at large-scale EUV and x-ray sources. The proliferation of these schemes based on laser-driven, tabletop implementations requires both high flux and circular polarization, two traditional challenges for HHG.

Here, we use circularly polarized high-harmonic radiation to reconstruct nanoscale magnetic structures by FTH and iterative phase retrieval for coherent diffractive imaging (CDI) (*33*). Specifically, we map worm-like magnetic domains in a cobalt/palladium (Co/Pd) multilayer stack using XMCD contrast within the cobalt M-edge spectral region (59-eV photon energy). We measure magneto-optical absorption and phase shifts with a spatial resolution down to 49 nm. The exceptional coherence of HHG allows us to enhance the magnetic signal using intense reference waves from tailored holographic masks.

EXPERIMENTAL SYSTEM

The experimental scheme is shown in Fig. 1: A pulsed laser beam from an amplified Ti:Sapphire laser system (pulse duration, 45 fs; repetition rate, 1 kHz; central wavelength, 800 nm; pulse energy, 2 mJ) is converted by an in-line "MAZEL-TOV" apparatus (*34*) to a beam with superimposed circularly polarized fundamental and second-harmonic fields of opposite helicities. This bichromatic laser field generates circularly polarized high harmonics in a He-filled gas cell (8 mm diameter, pressure of 500 mbar). The generation phase-matching conditions (*35*) are optimized by tuning the gas pressure, the position of the focus, and the laser confocal parameter. A 150-nm-thick Al foil blocks the bichromatic beam.

The imaging system comprises a toroidal diffraction grating, a slit, the sample, and a charge-coupled device (CCD) camera. The toroidal grating spatially disperses the harmonics and refocuses the selected 38th harmonic (21-nm wavelength, 59-eV photon energy) onto the sample. We optimize the rotation angle of the quarter-wave plate in the MAZEL-TOV device to achieve the correct selection rule for circularly polarized high-harmonic generation, which is evident from the suppression of every third harmonic order (*11*, *12*, *36*, *37*). The sample is a 200-nm-thick Si membrane, prepared with a magnetic multilayer Co/Pd stack on the front side. The magnetic film comprises nine pairs

[1]4th Physical Institute, University of Göttingen, Göttingen 37077, Germany. [2]Solid State Institute and Physics Department, Technion–Israel Institute of Technology, Haifa 32000, Israel. [3]1st Physical Institute, University of Göttingen, Göttingen 37077, Germany. [4]Institute of Physics, University of Augsburg, Augsburg 86159, Germany. [5]International Center for Advanced Studies of Energy Conversion (ICASEC), University of Göttingen, Göttingen, Germany.
*These authors contributed equally to this work.
†Corresponding author. Email: ofer.kfir@phys.uni-goettingen.de (O.K.); claus.ropers@uni-goettingen.de (C.R.)

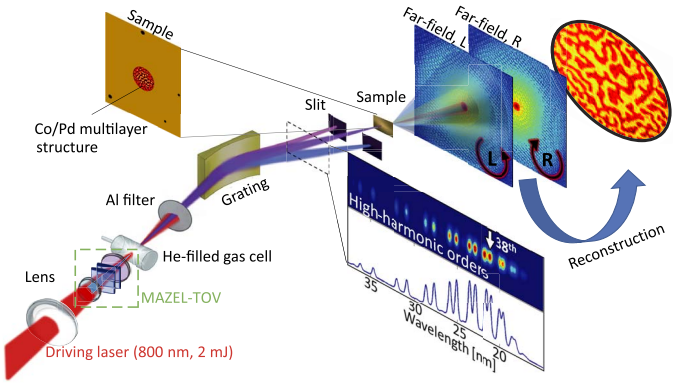

Fig. 1. A scheme of the experimental setup. A bichromatic circularly polarized beam tailored by a MAZEL-TOV apparatus generates circularly polarized high-order harmonics in a He-filled gas cell. The harmonics are spatially dispersed and refocused onto the sample by a single toroidal grating, and the 38th harmonic (marked on the spectrum) is selected by a slit. The scattering pattern from the sample is recorded with a CCD camera for left-hand (*L*) and right-hand (*R*) circular polarization of the high-harmonic beam. The magnetic domain pattern is retrieved from the two diffraction patterns by FTH and iterative phase retrieval. The sample (sketch, top left) shows the four reference holes and the worm-like domain structure on the central aperture.

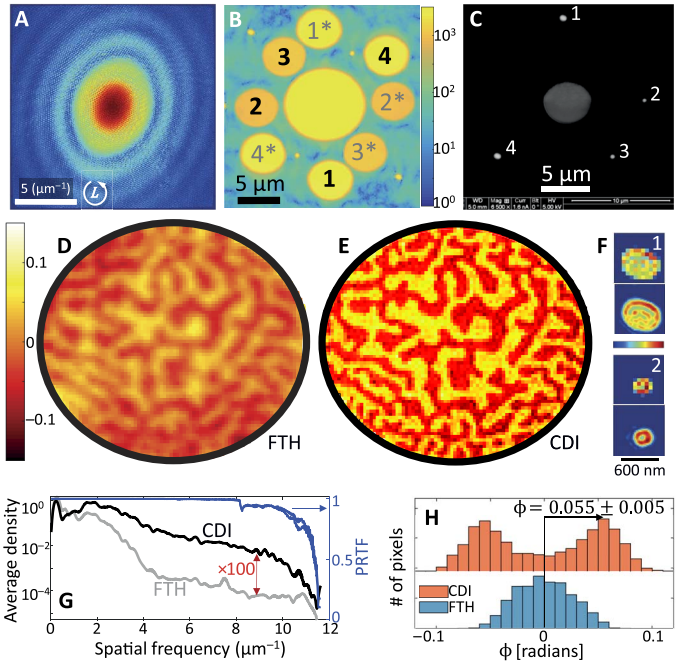

Fig. 2. Experimental results and the retrieval of nanoscale magnetic domain structure using high-order harmonics. (**A**) Diffraction pattern recorded with a left-hand circularly polarized 21-nm high-harmonic beam (logarithmic color scale, 341 s total integration time, 9×10^8 detected photons, corrected for spherical aberration by projection onto the Ewald sphere). (**B**) Fourier transform magnitude of the recorded diffraction pattern (logarithmic color scale). The holographic reconstructions from reference holes are marked 1 to 4 (conjugate holograms, 1* to 4*). (**C**) SEM micrograph of the gold-coated side of the sample, showing the central aperture (gray, 5 μm diameter) and four reference holes (white, numbered). (**D** and **E**) Magneto-optical phase-contrast images of the worm-like domain structure, obtained by FTH (reference hole 2, 250 nm diameter) and by CDI reconstruction, respectively (true pixel resolution, no interpolation). Positive (negative) phase indicates magnetization parallel (antiparallel) to the HHG beam. (**F**) Magnitude (linear scale, magnified) of the reconstructed exit waves of reference holes 1 and 2, at a true pixel resolution (top) and interpolated (bottom), illustrating the presence of high-order waveguide modes within the aperture. (**G**) Left axis: Fourier spectral density of phase-contrast images (azimuthally averaged). Right axis: Phase retrieval transfer functions (PRTFs) for independent reconstructions of left- and right-handed incident circular polarizations, demonstrating high fidelity of the CDI reconstructions. (**H**) Histogram of the measured phase, as reconstructed using CDI and FTH, allows quantitative evaluation of the magneto-optical phase.

of cobalt and palladium layers, $[Co(0.47\ nm)/Pd(0.75\ nm)]_9$, which results in worm-like magnetic domains with out-of-plane anisotropy after demagnetization (alternating external out-of-plane magnetic field of decreasing strength, see Materials and Methods). The backside of the substrate is covered with a 180-nm gold layer. Using focused ion beam etching, the EUV-opaque gold film is removed to form a central aperture. To complete the holographic mask, four reference holes with varying diameters are milled through the entire structure [see scanning electron microscopy (SEM) micrograph in Fig. 2C].

RESULTS AND DISCUSSION

Figure 2 displays the scattering data and reconstructions of the magnetic domain structure. The diffraction pattern recorded by illuminating the sample with a left-hand circularly polarized HHG beam is shown in Fig. 2A. For each reference hole, the Fourier transform of the diffraction pattern yields a holographic reconstruction of the complex wave exiting the central aperture (see, Fig. 2B, see also the Supplementary Materials). Individual reconstructions of the exit waves $f_{obj,L}(\mathbf{r})$ or $f_{obj,R}(\mathbf{r})$ for left-hand (*L*) or right-hand (*R*) circularly polarized illumination, respectively, exhibit a small magneto-optical signal on a large nonmagnetic background. Forming the ratio of the exit waves, we directly access the XMCD phase and absorption in a quantitative manner. The measured phase difference ϕ and amplitude ratio ρ are related to the magnetization component parallel to the beam, $M_z(\mathbf{r})$, integrated over the sample thickness, via

$$\frac{f_{obj,L}(\mathbf{r})}{f_{obj,R}(\mathbf{r})} = \exp\left[2ikd(\Delta\delta + i\Delta\beta)\left(\frac{M_z(\mathbf{r})}{|\mathbf{M}|}\right)\right] =: \rho e^{i\phi} \qquad (1)$$

(see details in Materials and Methods). Here, Δδ and Δβ are the dichroic refraction and absorption coefficients of cobalt (*32*), respectively; *k* is the wave number; *d* is the overall thickness of the magneto-optically active material (Co); and $|\mathbf{M}|$ is its saturation magnetization. Figure 2 (D and E) shows the XMCD phase-contrast images obtained by FTH and CDI reconstruction, respectively.

To retrieve the exit wave of our sample by CDI, we used an iterative "RAAR" algorithm (*38*), incorporating the FTH reconstruction for the real-space support and ensuring precise alignment of the two reconstructions (further details are given in Materials and Methods). The CDI reconstruction (Fig. 2E) yields a high-resolution refinement of the hologram, with sharp domain boundaries as well as a flat phase and amplitude within the domains. In addition, the reconstructed exit wave of the reference holes (Fig. 2F) includes multiple guided modes (*22*), with modulation at the level of a single pixel (60 nm in this case) corresponding to scattering that reaches the edges of the CCD detector. Thus, the diffracted reference field interferes with the object wave over the entire detector. An analysis of the azimuthally averaged spatial frequencies (Fig. 2G) of the reconstructions from FTH and CDI shows that the CDI phase map exhibits high-frequency components, which

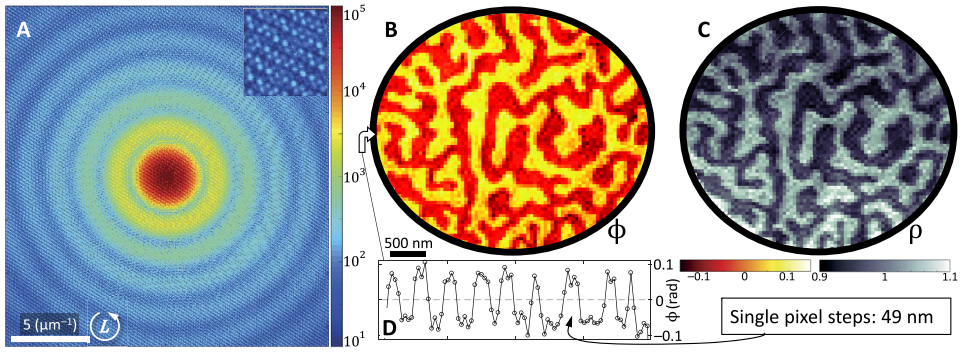

Fig. 3. Imaging of magnetic domains with 49-nm resolution. (**A**) Recorded diffraction pattern with high speckle visibility (see zoomed corner). Prominent diffraction rings arise from the four reference holes in the holographic mask (circular shape, diameter of ~600 nm). (**B** and **C**) CDI reconstructions of the magnetic domain structure with (B) phase and (C) amplitude magneto-optical contrast, respectively.

are damped in FTH by two orders of magnitude. Moreover, a broad peak around 1.7 μm^{-1} indicates a typical domain size of 300 nm. The phase retrieval transfer functions (PRTFs, blue curves in Fig. 2G) (*39*) demonstrate a reliable reconstruction throughout the detected diffraction pattern. The flat dichroic contrast within the reconstructed domains shows that the magnetization is locally saturated out-of-plane and oriented either parallel (bright contrast) or antiparallel (dark contrast) to the illuminating beam. This allows for a quantitative measurement of the dichroic phase, ϕ, and the magneto-optical phase coefficient $\Delta\delta$. From the histogram of measured phases (see Fig. 2H), we determine a dichroic phase shift of $\phi = 0.055 \pm 0.005$, corresponding to $\Delta\delta = 0.022 \pm 0.002$ for the given film thickness (see Materials and Methods for details). This value is larger than that obtained for free-standing cobalt (*32*) but consistent with measurements in multilayer stacks (*40*).

On the basis of this demonstration of diffraction-limited magnetic imaging, the spatial resolution can be further improved by detecting larger scattering angles. In Fig. 3, we present reconstructions of a different magnetic domain structure at a single-pixel, 49-nm resolution (object aperture, 4 μm; otherwise similar mask geometry). The recorded diffraction pattern (Fig. 3A; 600-s integration time) covers spatial frequencies up to 10.2 μm^{-1} (corner, 14.3 μm^{-1}) with high visibility across the CCD (see zoom of the top-right corner). The images of the dichroic phase and amplitude (Fig. 3, B and C) rival the quality and resolution of state-of-the-art experiments at FELs and synchrotrons (*41*, *42*) at an even larger field of view. The reconstructed images resolve curves, edges, and other fine features of the domains. Again, diffraction-limited resolution is achieved, as evident from the step-like contrast changes between adjacent domains (lineout in Fig. 3D).

Our analysis illustrates that applying CDI to a data set with holographic information is advantageous on multiple levels (*43*, *44*), especially for weakly scattering objects, as in XMCD. First, the hologram assists a rapid convergence of the iterative algorithm, with additional redundancy provided by multiple reference holes of varying sizes. This results in an unambiguous CDI reconstruction directly validated by FTH (*21*). Second, the hologram provides for a data-based support of the exit wave, accurate to the size of the smallest reference hole. This may be particularly useful for structures with a complicated support. Third, the signal from a weakly scattering object is enhanced by the interference with a strong reference wave, which enables a CDI reconstruction. Finally, while FTH resolution suffers for larger reference holes, the CDI algorithm is fully capable of reconstructing their complex exit-wave patterns, leading to a diffraction-limited resolution. Specifically, guided modes with high spatial frequencies suffer less attenuation upon propagation in wider reference holes (*22*) and thus can enhance the high-resolution information at large spatial frequencies. In these experiments, the scattering from large reference holes provides substantial diffraction intensity across the detector (see rings in Figs. 2A and 3A), which is instrumental for reconstructing the weak magneto-optical scattering with diffraction-limited resolution.

In conclusion, this work reports the first nanoscale magnetic imaging with high-order harmonic radiation. We use circularly polarized illumination to map a randomly formed magnetic domain pattern, and reach a spatial resolution of 49 nm by CDI. Our experiment shows that for weakly scattering objects, structured reference waves contribute to the robustness, stability, and resolution of CDI phase retrieval. This approach can be further developed to achieve resolutions of 10 nm and less, for example, by using recently developed keV-scale high-harmonic sources (*45*–*47*) to access L-edge XMCD contrast. The discrete harmonic spectrum may also allow an extension to hyperspectral imaging (*42*, *48*, *49*), facilitating multiple-element contrast and the investigation of spatiotemporal dynamics in magnetic heterostructures or skyrmion systems. Besides applications in magnetism, we believe that tabletop nanoimaging based on circularly polarized high-harmonic radiation will contribute to the fundamental understanding of microscopic chiral phenomena.

MATERIALS AND METHODS

Sample preparation

The multilayer stack, Pd(2 nm)/[Co(0.47 nm)/Pd(0.75 nm)]$_9$/Pd(2 nm)/Cr(1.5 nm), was deposited via dc magnetron sputtering at room temperature at an Ar partial pressure of 4.5 mtorr. The thicknesses of the individual materials were precalibrated by x-ray reflectometry. Here, Cr was an adhesion layer, followed by a Pd layer that promoted a (111) texture of the Co/Pd multilayers. A Pd cap layer provided an oxidation barrier. The substrate was the front side of a 200-nm-thick Si membrane, whereas the central aperture and the reference holes were milled from the Au-coated backside (180 nm). A typical worm-like domain pattern (*50*) was formed by saturating the out-of-plane magnetization in an external field, followed by a set of field polarity inversions, with a reduced field magnitude by 15% in each inversion.

Data acquisition

For the data in Fig. 2, two individual diffraction patterns (exposure times of 330 and 11 s) were recorded with a CCD camera (1340 × 1300 pixels, 20 μm pixel size) for each helicity. Combining the diffraction patterns of

these two exposure times increased the total dynamic range of the diffraction pattern. After a dark image subtraction, the left- and right-handed circularly polarized diffraction patterns were centered and mapped onto the Ewald sphere to account for spherical aberrations induced by the flat CCD detector. The real-space support for the iterative phase retrieval process was derived by thresholding the inverse Fourier transformation of the measured far-field intensities (Fig. 2B) and subsequent deconvolution of the object's support from its autocorrelation. The data in Fig. 3 were recorded using the same approach. The scattering patterns were acquired for 600 s per helicity, and the overexposed central part was replaced with the data from diffraction patterns composed of 30 accumulations with 6-s exposure time each. The central aperture in the holographic mask had a diameter of 4 μm. The reference holes were equidistantly displaced 6.6 μm away from the center of the aperture and had circular shapes with diameters of ~600 nm. The diffraction patterns, as used for the reconstruction, are presented in fig. S1. The top row shows the diffraction recorded with left-handed (*L*) and right-handed (*R*) circularly polarized HHG for the data presented in Fig. 2, and the bottom row shows the diffraction patterns for the data presented in Fig. 3.

Iterative phase retrieval

For the reconstructions, we used 1000 RAAR (*38*) iterations (200 iterations with $\beta = 0.99$, 200 iterations with a gradual decrease of β to 0.5, and 600 iterations with $\beta = 0.5$). For each helicity, we analyzed the fidelity of the result using the PRTF (*39*) for 20 individual reconstructions starting from random initial guesses. We used a definition of the PRTF that is the average over the phase terms of all independent reconstructions, $\langle \exp[i\psi] \rangle$. Figure S2 presents the azimuthal averages for the reconstruction in Figs. 2 and 3, supporting spatial frequencies up to 11.36 and 11.14 μm^{-1}, corresponding to resolutions of 44 and 45 nm, respectively. We note that the PRTF is also often defined somewhat differently [by Chapman *et al.* (*51*) and Shapiro *et al.* (*52*)], which yields very similar results.

To precisely align the reconstructions from left- and right-handed illumination, we developed a method appropriate for dichroic imaging: First, the spectral phase was retrieved iteratively only for one diffraction pattern, say, for left-handed illumination (*L*). Second, the right-handed diffraction was overlaid with the retrieved phase of the left-handed phase. This step matched the global phase and phase gradients between the far-fields of the two illumination helicities (that is, phase and positioning in the real-space reconstruction). Very few RAAR iterations (20 iterations, $\beta = 0.5$) retrieved the far-field phase to match the right-handed recorded diffraction. The dichroic phase (ϕ) and amplitude images (ρ), were plotted and quantitatively evaluated.

Quantitative estimation of the magneto-optical coefficient, Δδ

The magneto-optical activity of cobalt is expressed in the refractive index (*32*), $n_{\pm} = (1 - (\delta \pm \Delta\delta)) - i(\beta \pm \Delta\beta)$. The magneto-optical refraction coefficients are proportional to the magnetization projected onto the optical axis (*53*), $M_z/|\mathbf{M}|$, so that for left-hand circular polarization, parallel/antiparallel magnetization acquires a +/− sign. Thus, a plane wave transmitted through a magnetic sample results in the exit wave $f_{\text{exit},\,L/R} = e^{-ikdn_{\pm}} = e^{-kd(\beta \pm \Delta\beta)} e^{-ikd(1-(\delta \pm \Delta\delta))}$. Equation 1 was retrieved by dividing the exit waves for left-hand (*L*) and right-hand (*R*) circular polarizations, and accounting for the magnetization strength and orientation, $M_z/|\mathbf{M}|$. For locally saturated magnetization parallel or antiparallel to the beam, the magneto-optical refraction is $\Delta\delta = \phi/2kd$, where ϕ is the measured dichroic phase shift. From the peaks of the phase-contrast histogram (Fig. 2H), the dichroic phase shift is $\phi = 0.055 \pm 0.005$. Considering the total thickness of the cobalt layers, $d_{Co} = 4.23$ nm ($kd_{Co} = 1.26$), the magneto-optical refraction is $\Delta\delta = 0.022 \pm 0.002$. Our estimation for $\Delta\delta$ assumed that the illumination is purely circularly polarized and that the magnetization in the fully saturated regions was exactly parallel/antiparallel to the beam.

SUPPLEMENTARY MATERIALS

Supplementary material for this article is available at http://advances.sciencemag.org/cgi/content/full/3/12/eaao4641/DC1

fig. S1. Diffraction patterns for left- and right-handed circularly polarized HHG for the reconstructions presented in Figs. 2 and 3.

fig. S2. Azimuthally averaged PRTF for the data presented in Figs. 2 and 3.

fig. S3. Amplitude and phase maps to complement the phase images in Fig. 2.

fig. S4. The reconstructed wave exiting the reference holes, partly presented in Fig. 2F.

References (*54*, *55*)

REFERENCES AND NOTES

1. S. Mühlbauer, B. Binz, F. Jonietz, C. Pfleiderer, A. Rosch, A. Neubauer, R. Georgii, P. Böni, Skyrmion lattice in a chiral magnet. *Science* **323**, 915–919 (2009).
2. A. Soumyanarayanan, N. Reyren, A. Fert, C. Panagopoulos, Emergent phenomena induced by spin–orbit coupling at surfaces and interfaces. *Nature* **539**, 509–517 (2016).
3. J. Stöhr, H. C. Siegmann, *Magnetism: From Fundamentals to Nanoscale Dynamics* (Springer Berlin, 2006).
4. R. E. Dunin-Borkowski, M. R. McCartney, R. B. Frankel, D. A. Bazylinski, M. Pósfai, P. R. Buseck, Magnetic microstructure of magnetotactic bacteria by electron holography. *Science* **282**, 1868–1870 (1998).
5. A. Krasyuk, A. Oelsner, S. A. Nepijko, A. Kuksov, C. M. Schneider, G. Schönhense, Time-resolved photoemission electron microscopy of magnetic field and magnetisation changes. *Appl. Phys. A Mater.* **76**, 863–868 (2003).
6. Y. Zhu, *Modern Techniques for Characterizing Magnetic Materials* (Springer Science & Business Media, 2005).
7. B. Van Waeyenberge, A. Puzic, H. Stoll, K. W. Chou, T. Tyliszczak, R. Hertel, M. Fähnle, H. Brückl, K. Rott, G. Reiss, I. Neudecker, D. Weiss, C. H. Back, G. Schütz, Magnetic vortex core reversal by excitation with short bursts of an alternating field. *Nature* **444**, 461–464 (2006).
8. P. A. Midgley, R. E. Dunin-Borkowski, Electron tomography and holography in materials science. *Nat. Mater.* **8**, 271–280 (2009).
9. A. Kirilyuk, A. V. Kimel, T. Rasing, Ultrafast optical manipulation of magnetic order. *Rev. Mod. Phys.* **82**, 2731–2784 (2010).
10. F. Büttner, C. Moutafis, M. Schneider, B. Krüger, C. M. Günther, J. Geilhufe, C. v. Korff Schmising, J. Mohanty, B. Pfau, S. Schaffert, A. Bisig, M. Foerster, T. Schulz, C. A. F. Vaz, J. H. Franken, H. J. M. Swagten, M. Kläui, S. Eisebitt, Dynamics and inertia of skyrmionic spin structures. *Nat. Phys.* **11**, 225–228 (2015).
11. A. Fleischer, O. Kfir, T. Diskin, P. Sidorenko, O. Cohen, Spin angular momentum and tunable polarization in high-harmonic generation. *Nat. Photonics* **8**, 543–549 (2014).
12. O. Kfir, P. Grychtol, E. Turgut, R. Knut, D. Zusin, D. Popmintchev, T. Popmintchev, H. Nembach, J. M. Shaw, A. Fleischer, H. Kapteyn, M. Murnane, O. Cohen, Generation of bright phase-matched circularly-polarized extreme ultraviolet high harmonics. *Nat. Photonics* **9**, 99–105 (2015).
13. A. McPherson, G. Gibson, H. Jara, U. Johann, T. S. Luk, I. A. McIntyre, K. Boyer, C. K. Rhodes, Studies of multiphoton production of vacuum-ultraviolet radiation in the rare gases. *J. Opt. Soc. Am. B* **4**, 595–601 (1987).
14. R. A. Bartels, A. Paul, H. Green, H. C. Kapteyn, M. M. Murnane, S. Backus, I. P. Christov, Y. Liu, D. Attwood, C. Jacobsen, Generation of spatially coherent light at extreme ultraviolet wavelengths. *Science* **297**, 376–378 (2002).
15. M. Hentschel, R. Kienberger, Ch. Spielmann, G. A. Reider, N. Milosevic, T. Brabec, P. Corkum, U. Heinzmann, M. Drescher, F. Krausz, Attosecond metrology. *Nature* **414**, 509–513 (2001).
16. M. Chini, K. Zhao, Z. Chang, The generation, characterization and applications of broadband isolated attosecond pulses. *Nat. Photonics* **8**, 178–186 (2014).
17. S. Mathias, C. La-o-vorakiat, J. M. Shaw, E. Turgut, P. Grychtol, R. Adam, D. Rudolf, H. T. Nembach, T. J. Silva, M. Aeschlimann, C. M. Schneider, H. C. Kapteyn, M. M. Murnane, Ultrafast element-specific magnetization dynamics of complex magnetic materials on a table-top. *J. Electron Spectros. Relat. Phenomena* **189**, 164–170 (2013).

18. Y. Pertot, C. Schmidt, M. Matthews, A. Chauvet, M. Huppert, V. Svoboda, A. von Conta, A. Tehlar, D. Baykusheva, J.-P. Wolf, H. J. Wörner, Time-resolved x-ray absorption spectroscopy with a water window high-harmonic source. *Science* **355**, 264–267 (2017).
19. C. Benko, T. K. Allison, A. Cingöz, L. Hua, F. Labaye, D. C. Yost, J. Ye, Extreme ultraviolet radiation with coherence time greater than 1 s. *Nat. Photonics* **8**, 530–536 (2014).
20. R. L. Sandberg, A. Paul, D. A. Raymondson, S. Hädrich, D. M. Gaudiosi, J. Holtsnider, R. I. Tobey, O. Cohen, M. M. Murnane, H. C. Kapteyn, C. Song, J. Miao, Y. Liu, F. Salmassi, Lensless diffractive imaging using tabletop coherent high-harmonic soft-x-ray beams. *Phys. Rev. Lett.* **99**, 098103 (2007).
21. R. L. Sandberg, D. A. Raymondson, C. La-o-vorakiat, A. Paul, K. S. Raines, J. Miao, M. M. Murnane, H. C. Kapteyn, W. F. Schlotter, Tabletop soft-x-ray Fourier transform holography with 50 nm resolution. *Opt. Lett.* **34**, 1618–1620 (2009).
22. S. Zayko, E. Mönnich, M. Sivis, D.-D. Mai, T. Salditt, S. Schäfer, C. Ropers, Coherent diffractive imaging beyond the projection approximation: Waveguiding at extreme ultraviolet wavelengths. *Opt. Express* **23**, 19911–19921 (2015).
23. J. Miao, T. Ishikawa, I. K. Robinson, M. M. Murnane, Beyond crystallography: Diffractive imaging using coherent x-ray light sources. *Science* **348**, 530–535 (2015).
24. J. C. H. Spence, U. Weierstall, M. Howells, Coherence and sampling requirements for diffractive imaging. *Ultramicroscopy* **101**, 149–152 (2004).
25. J. Miao, T. Ishikawa, E. H. Anderson, K. O. Hodgson, Phase retrieval of diffraction patterns from noncrystalline samples using the oversampling method. *Phys. Rev. B.* **67**, 174104 (2003).
26. S. Zayko, M. Sivis, S. Schäfer, C. Ropers, Polarization contrast of nanoscale waveguides in high harmonic imaging. *Optica* **3**, 239–242 (2016).
27. B. Vodungbo, J. Gautier, G. Lambert, A. B. Sardinha, M. Lozano, S. Sebban, M. Ducousso, W. Boutu, K. Li, B. Tudu, M. Tortarolo, R. Hawaldar, R. Delaunay, V. López-Flores, J. Arabski, C. Boeglin, H. Merdji, P. Zeitoun, J. Lüning, Laser-induced ultrafast demagnetization in the presence of a nanoscale magnetic domain network. *Nat. Commun.* **3**, 999 (2012).
28. P. Fischer, Frontiers in imaging magnetism with polarized x-rays. *Front. Phys.* **2**, **82** (2015).
29. G. Meier, M. Bolte, R. Eiselt, B. Krüger, D.-H. Kim, P. Fischer, Direct imaging of stochastic domain-wall motion driven by nanosecond current pulses. *Phys. Rev. Lett.* **98**, 187202 (2007).
30. S. Eisebitt, J. Lüning, W. F. Schlotter, M. Lörgen, O. Hellwig, W. Eberhardt, J. Stöhr, Lensless imaging of magnetic nanostructures by X-ray spectro-holography. *Nature* **432**, 885–888 (2004).
31. I. McNulty, J. Kirz, C. Jacobsen, E. H. Anderson, M. R. Howells, D. P. Kern, High-resolution imaging by Fourier transform X-ray holography. *Science* **256**, 1009–1012 (1992).
32. S. Valencia, A. Gaupp, W. Gudat, H.-Ch. Mertins, P. M. Oppeneer, D. Abramsohn, C. M. Schneider, Faraday rotation spectra at shallow core levels: 3*p* edges of Fe, Co, and Ni. *New J. Phys.* **8**, 254 (2006).
33. J. Miao, P. Charalambous, J. Kirz, D. Sayre, Extending the methodology of x-ray crystallography to allow imaging of micrometre-sized non-crystalline specimens. *Nature* **400**, 342–344 (1999).
34. O. Kfir, E. Bordo, G. I. Haham, O. Lahav, A. Fleischer, O. Cohen, In-line production of a bi-circular field for generation of helically polarized high-order harmonics. *Appl. Phys. Lett.* **108**, 211106 (2016).
35. T. Popmintchev, M.-C. Chen, P. Arpin, M. M. Murnane, H. C. Kapteyn, The attosecond nonlinear optics of bright coherent x-ray generation. *Nat. Photonics* **4**, 822–832 (2010).
36. S. Long, W. Becker, J. K. McIver, Model calculations of polarization-dependent two-color high-harmonic generation. *Phys. Rev. A* **52**, 2262–2278 (1995).
37. H. Eichmann, A. Egbert, S. Nolte, C. Momma, B. Wellegehausen, W. Becker, S. Long, J. K. McIver, Polarization-dependent high-order two-color mixing. *Phys. Rev. A* **51**, R3414–R3417 (1995).
38. D. R. Luke, Relaxed averaged alternating reflections for diffraction imaging. *Inverse Probl.* **21**, 37 (2005).
39. S. Marchesini, H. N. Chapman, A. Barty, C. Cui, M. R. Howells, J. C. H. Spence, U. Weierstall, A. M. Minor, Phase aberrations in diffraction microscopy. http://arxiv.org/abs/physics/0510033 (2005).
40. K. Saito, M. Igeta, T. Ejima, T. Hatano, A. Arai, M. Watanabe, Magnetic rotation spectra of Co/Pt and Co/Cu multilayers in 50–90 eV region. *J. Electron Spectros. Relat. Phenomena* **144–147**, 757–760 (2005).
41. S. Schaffert, B. Pfau, J. Geilhufe, C. M. Günther, M. Schneider, C. von Korff Schmising, S. Eisebitt, High-resolution magnetic-domain imaging by Fourier transform holography at 21 nm wavelength. *New J. Phys.* **15**, 093042 (2013).
42. F. Willems, C. von Korff Schmising, D. Weder, C. M. Günther, M. Schneider, B. Pfau, S. Meise, E. Guehrs, J. Geilhufe, A. E. D. Merhe, E. Jal, B. Vodungbo, J. Lüning, B. Mahieu, F. Capotondi, E. Pedersoli, D. Gauthier, M. Manfredda, S. Eisebitt, Multi-color imaging of magnetic Co/Pt heterostructures. *Struct. Dyn.* **4**, 014301 (2017).
43. S. Hoffmann-Urlaub, T. Salditt, Miniaturized beamsplitters realized by x-ray waveguides. *Acta Crystallogr. A Found. Adv.* **72**, 515–522 (2016).
44. T. Latychevskaia, J.-N. Longchamp, H.-W. Fink, When holography meets coherent diffraction imaging. *Opt. Express* **20**, 28871–28892 (2012).
45. T. Popmintchev, M.-C. Chen, D. Popmintchev, P. Arpin, S. Brown, S. Ališauskas, G. Andriukaitis, T. Balčiunas, O. D. Mücke, A. Pugzlys, A. Baltuška, B. Shim, S. E. Schrauth, A. Gaeta, C. Hernández-García, L. Plaja, A. Becker, A. Jaron-Becker, M. M. Murnane, H. C. Kapteyn, Bright coherent ultrahigh harmonics in the keV x-ray regime from mid-infrared femtosecond lasers. *Science* **336**, 1287–1291 (2012).
46. J. Li, X. Ren, Y. Yin, Y. Cheng, E. Cunningham, Y. Wu, Z. Chang, Polarization gating of high harmonic generation in the water window. *Appl. Phys. Lett.* **108**, 231102 (2016).
47. S. L. Cousin, F. Silva, S. Teichmann, M. Hemmer, B. Buades, J. Biegert, High-flux table-top soft x-ray source driven by sub-2-cycle, CEP stable, 1.85-μm 1-kHz pulses for carbon K-edge spectroscopy. *Opt. Lett.* **39**, 5383–5386 (2014).
48. S. Witte, V. T. Tenner, D. W. E. Noom, K. S. E. Eikema, Lensless diffractive imaging with ultra-broadband table-top sources: From infrared to extreme-ultraviolet wavelengths. *Light Sci. Appl.* **3**, e163 (2014).
49. Y. Meng, C. Zhang, C. Marceau, A. Y. Naumov, P. B. Corkum, D. M. Villeneuve, Octave-spanning hyperspectral coherent diffractive imaging in the extreme ultraviolet range. *Opt. Express* **23**, 28960–28969 (2015).
50. R. Sbiaa, M. Ranjbar, J. Åkerman, Domain structures and magnetization reversal in Co/Pd and CoFeB/Pd multilayers. *J. Appl. Phys.* **117**, 17C102 (2015).
51. H. N. Chapman, A. Barty, S. Marchesini, A. Noy, S. P. Hau-Riege, C. Cui, M. R. Howells, R. Rosen, H. He, J. C. H. Spence, U. Weierstall, T. Beetz, C. Jacobsen, D. Shapiro, High-resolution ab initio three-dimensional x-ray diffraction microscopy. *J. Opt. Soc. Am. A Opt. Image Sci. Vis.* **23**, 1179–1200 (2006).
52. D. Shapiro, P. Thibault, T. Beetz, V. Elser, M. Howells, C. Jacobsen, J. Kirz, E. Lima, H. Miao, A. M. Neiman, D. Sayre, Biological imaging by soft x-ray diffraction microscopy. *Proc. Natl. Acad. Sci. U.S.A.* **102**, 15343–15346 (2005).
53. L. D. Landau, J. S. Bell, M. J. Kearsley, L. P. Pitaevskii, E.M. Lifshitz, J. B. Sykes, *Electrodynamics of Continuous Media* (Elsevier, ed. 2, 2013).
54. B. E. A. Saleh, M. C. Teich, *Fundamentals of Photonics* (Wiley, ed. 2, 2013).
55. A. Yariv, P. Yeh, *Photonics: Optical Electronics in Modern Communications* (Oxford Univ. Press, 2007).

Acknowledgments: We gratefully acknowledge discussions and support from T. Salditt, C. Lienau, and H. Kollmann. **Funding:** This work was funded by the Deutsche Forschungsgemeinschaft (DFG) within SFB 755 "Nanoscale photonic imaging" (project C08). O.K. acknowledges funding from the European Union's Horizon 2020 research and innovation programme under the Marie Skłodowska-Curie grant agreement no. 752533.
Author contributions: O.K. and S.Z. planned and constructed the experimental setup, performed the experiments, and analyzed the data, with contributions from M.S. and C.N. The sample was designed by O.K., S.Z., C.N., M.S., B.H., S.S.P.K.A., and M.A. and prepared by S.S.P.K.A. Mask preparation and SEM were carried out by M.M. and M.S. The manuscript was written by O.K., S.Z., and C.R. with input from all authors. The project was conceived and supervised by C.R. with contributions from S.S., D.S., S.M., and O.C. **Competing interests:** The authors declare that they have no competing interests. **Data and materials availability:** All data needed to evaluate the conclusions in the paper are present in the paper and/or the Supplementary Materials. Additional data related to this paper may be requested from the authors.

Submitted 24 July 2017
Accepted 15 November 2017
Published 15 December 2017
10.1126/sciadv.aao4641

Citation: O. Kfir, S. Zayko, C. Nolte, M. Sivis, M. Möller, B. Hebler, S. S. P. K. Arekapudi, D. Steil, S. Schäfer, M. Albrecht, O. Cohen, S. Mathias, C. Ropers, Nanoscale magnetic imaging using circularly polarized high-harmonic radiation. *Sci. Adv.* **3**, eaao4641 (2017).